SANDIA REPORT
SAND2006-7235
Unlimited Release
Printed November 2006

Microwave to Millimeter-wave Electrodynamic Response and Applications of Semiconductor Nanostructures: LDRD Project 67025 Final Report

Mark Lee, Eric A. Shaner, Clark Highstrete, John L. Reno, Michael C. Wanke, S. James Allen, W. J. Padilla, R. D. Averitt and A. J. Taylor

Prepared by
Sandia National Laboratories
Albuquerque, New Mexico 87185 and Livermore, California 94550

Sandia is a multiprogram laboratory operated by Sandia Corporation,
a Lockheed Martin Company, for the United States Department of Energy's
National Nuclear Security Administration under Contract DE-AC04-94AL85000.

Issued by Sandia National Laboratories, operated for the United States Department of Energy by Sandia Corporation.

Available to DOE and DOE contractors from
U.S. Department of Energy
Office of Scientific and Technical Information
P.O. Box 62
Oak Ridge, TN 37831

Telephone: (865) 576-8401
Facsimile: (865) 576-5728
E-Mail: reports@adonis.osti.gov
Online ordering: http://www.osti.gov/bridge

Available to the public from
U.S. Department of Commerce
National Technical Information Service
5285 Port Royal Rd.
Springfield, VA 22161

Telephone: (800) 553-6847
Facsimile: (703) 605-6900
E-Mail: orders@ntis.fedworld.gov
Online order: http://www.ntis.gov/help/ordermethods.asp?loc=7-4-0#online

SAND 2006-7235
Unlimited Release
Printed November 2006

Microwave to Millimeter-wave Electrodynamic Response and Applications of Semiconductor Nanostructures: LDRD Project 67025 Final Report

Mark Lee, Eric A. Shaner, and Clark Highstrete
Semiconductor Materials and Device Sciences Department

John L. Reno
CINT Science Department

Michael C. Wanke
Photonic Microsystems Technology Department

Sandia National Laboratories
P.O. Box 5800
Albuquerque, NM 87185-1415

S. James Allen
University of California Santa Barbara
Santa Barbara, CA 93106

W. J. Padilla, R. D. Averitt, A. J. Taylor
Los Alamos National Laboratory
Los Alamos, New Mexico 87545

Abstract

LDRD Project 67025 provided support to pursue experiments studying the electrodynamic response and possible applications of various innovative semiconductor-based nanostructures from microwave (approximately 1 GHz) up to millimeter- and submillimeter-wave (several hundred GHz) frequencies. Under this project, the non-linear behavior of plasmons in a high-mobility GaAs-AlGaAs quantum-well field-effect transistor was studied up to 145 GHz using difference frequency mixing techniques. Applications of such a plasmon transistor as a millimeter-wave mixer receiver were investigated. Also, negative refractive-index metamaterials consisting of arrays of split-ring resonators were fabricated and their transmission resonance spectra measured from 50 to 2000 GHz. High quality factor resonances with large negative index were observed, and applications as a tunable filter or modulator investigated.

Contents

1. Introduction

The research done under this LDRD was to characterize the unique electrodynamic properties of semiconductor nanostructures at microwave to millimeter-wave frequencies, roughly one to several hundred GHz, and to explore applications of the knowledge gained to innovative high-frequency devices having radically superior performance resulting explicitly from nano-scale or quantum effects. Specifically, we have worked with quantum-well field-effect transistors fabricated from a high-mobility two-dimensional electron gas (2DEG) in a GaAs-AlGaAs semiconductor heterostructure. Such structures were found to respond to high-frequency electromagnetic fields via collective excitation of charge density oscillations, or plasmons, rather than ordinary electrons. Such an effect is marked by distinctive electrically tunable resonances that can be used to detect and manipulate high-frequency signals. In addition, we have fabricated and investigated the anomalous dispersion and negative index-of-refraction resonances in arrays of split ring resonators (SRRs) patterned on high-purity GaAs. Very high quality factor resonances were achieved that allowed large negative refraction index values to be obtained. These negative index resonances can be dynamically suppressed via ultra-fast infrared pulses generating free carriers in the GaAs substrate. Such dynamic resonance suppression makes possible optically tunable filters and fast modulators for microwave and millimeter-wave electromagnetic signals.

2. Frequency mixing in a plasmon quantum-well field-effect transistor

Coherent charge density oscillations (plasmons) in a high-mobility two-dimensional electron gas (2DEG) could be exploited to circumvent physical limits on maximum operating frequency in conventional devices based on electron drift. This speed increase arises from the fact that 2DEG plasmons have velocities ~ 10^8 cm/s, roughly ten times faster than uncorrelated electron drift, hence reducing charge transit time between source and drain contacts. Typical 2DEG densities from 10^{10} to 10^{12} cm^{-2} yield plasmon frequencies in the 100 GHz to 1 THz range, making plasmon devices attractive for THz applications. In addition, the ability to electrically tune the 2DEG charge density and hence the plasmon resonance via a gate voltage in a field effect transistor (FET) offers highly desirable new functionalities, such as "spectrometer-on-a-chip" capability.

Plasmon resonance effects in semiconductor hetero-structures have been observed for many years. [1,2] Indeed, the microwave conductivity of a gated high-mobility 2DEG has been described as the circuit equivalent of a 2D plasmon. [3] For device applications, Dyakonov and Shur [4,5] provided a physical model and calculation framework for various plasmon functionalities in high electron mobility transistors (HEMTs). Popov, *et al*. [6] analyzed in detail absorption by plasmons in a quantum well THz direct detector. Only recently have empirical demonstrations of plasmon devices been reported. These have included a THz oscillator using an InGaAs-based HEMT, [7] and various forms of direct detectors such as a GaAs-AlGaAs double-quantum-well (DQW) FET, [8] various III-V HEMTs, [9,10,11] and a silicon FET. [12]

Here we present an experimental report on heterodyne mixing in a plasmon-based device. The mixer is a grating-gated GaAs-AlGaAs DQW FET designed to have plasmon resonances between 100 to 200 GHz. The mixing response is found to have two distinct regimes dependent on 2DEG density via the gate bias. Very close to pinch-off the device exhibits a broadband response which is well-described by a simple bolometric mechanism. The conducting regime shows a gate-tunable plasmon resonance that has more complicated nonlinear behavior than a bolometer. In either regime the intermediate frequency (IF) bandwidth can be fairly wide, > 2 GHz for resonant plasmon mixing.

The grating-gated DQW FET has the same basic design as described in detail in Ref. 8, where direct detection resonances from 570 to 660 GHz were shown. The main difference between the device used here from that of Ref. 8 is that the period of the grating gate here is 16 μm (8 μm metal / 8 μm gap) rather than 4 μm. The larger grating period selects out longer wavelength plasmon modes consistent with our 94 to 145 GHz mixing measurements. Otherwise, the composition of the DQW heterostructures are the same, *i.e.* two 20 nm wide GaAs QWs, modulation doped at 1.7 x 10^{11} cm^{-2} (upper QW) and 2.6 x 10^{11} cm^{-2} (lower QW) separated by a 7 nm AlGaAs barrier. The device area covered by the grating gate was 2 mm x 2 mm. At 4 K the Hall mobility of the composite heterostructure was $\mu \approx 1.7 \times 10^6$ $cm^2/V{\cdot}s$, giving a momentum relaxation time $\tau = m^*\mu/e \approx 65$ ps and an elastic mean free path at 4 K exceeding 10 μm, so electrons transit the ungated 8 μm gaps beneath the gate grating electrodes in a semiclassical

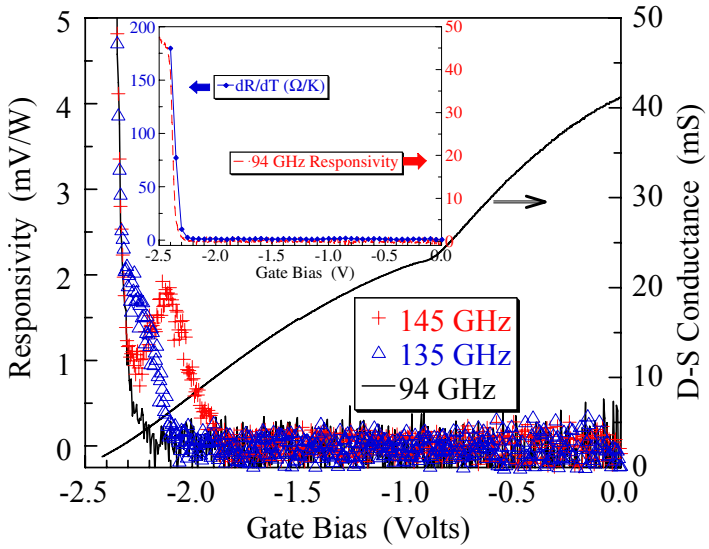

FIG. 1. Drain-source conductance and responsivity with 10 μA bias in response to 94, 135, and 145 GHz radiation, as a function of the gate bias. The kink in the conductance at -0.8 V is the depletion of the upper. Inset: Responsivity at 94 GHz and the temperature slope of the drain-source resistance dR_{DS}/dT plotted against gate bias at 4 K.

ballistic manner. [13] Fig. 4 shows drain-source conductance vs. gate bias. Pinch-off occurs near –0.8 V gate bias in the upper QW and around –2.45 V in the lower QW.

For the mixing measurements, a DQW FET was attached to a 4 K cryostat plate behind a cold long-wavelength pass filter and a Teflon window. The gate-source was biased between 0 to –2.5 V, and gate leakage was < 10 pA even at the most negative gate bias. The drain-source was dc biased at 10 μA through a wideband bias tee. Local oscillator (LO) and signal (rf) radiation was provided by a pair of Gunn oscillators (maximum output power 35 mW) focused through a 300 mm diameter Gaussian lens antenna to a beam waist diameter of ~ 5 mm. Polarization was orthogonal to the gate grating lines. Attenuation was adjusted so that 0.1 to 1 mW of LO power and 1 to 10 μW of rf power were incident at the sample plane as measured by a power meter set at the sample position inside the cryostat. The difference frequency (IF) generated by the mixer was output through the bias tee to a low-noise amplifier mounted on the 4 K plate and measured by a spectrum analyzer. The instrumental IF bandwidth was 2 GHz, limited by the amplifier and the reactance from a parasitic inductance of a wire bond contact.

Fig. 1 shows the direct detection responsivity as a function of gate bias V_g at three different LO frequencies, 94, 135, and 145 GHz. The responsivity shown is the change in

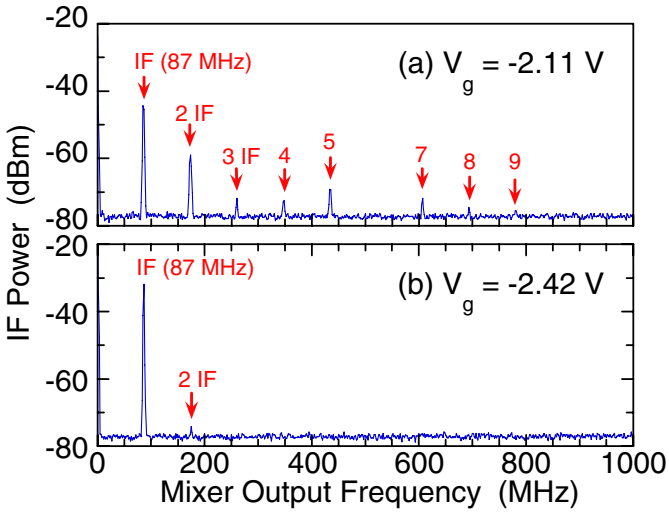

FIG. 2. Power spectrum of the IF output with a rf of 145 GHz and fixed 87 MHz IF. All measurement parameters are held constant except that in (a) the gate bias is held at the peak of the 145 GHz plasmon resonance response, while in (b) the gate bias is held in the broadband pinch-off response. Harmonics of the fundamental IF are indicated.

drain-source voltage δV_{ds} at the 37 Hz chopping rate of the incoming LO radiation divided by the nominal LO power incident at the sample position. Two different response regimes are evident. Above pinch-off, a clear resonant response to 145 GHz is centered at $V_g = -2.11$ V, the signature of a plasmon excitation in the same manner as reported in Ref. 8 and analyzed in Ref. 6. The resonant responsivity magnitude is ~2 mV/W, uncorrected for the fact that the device area is smaller than the nominal beam waist. At slightly more negative gate bias, *i.e.* lower 2DEG density, a partial resonance peak in response to 135 GHz is apparent at $V_g \approx -2.25$ V, barely above pinch-off. This resonance redshift is consistent with the decrease in 2DEG density. No resonance in response to 94 GHz is seen as the gate bias required is below pinch-off. Pinched off at $V_g < -2.4$ V, the responsivity curves for all three frequencies share a common, large rise that goes up to almost 50 mV/W independent of frequency. This larger responsivity near pinch-off is thus broadband.

The resonant plasmon and broadband pinch-off regimes have very distinct mixing characteristics. Fig. 2 shows spectra of the IF power generated by the mixer for a 145 GHz rf signal and a LO detuned to give a fundamental IF of 87 MHz. Fig. 2(a) shows the spectrum with $V_g = -2.11$ V, the peak of the 145 GHz plasmon. This spectrum shows a

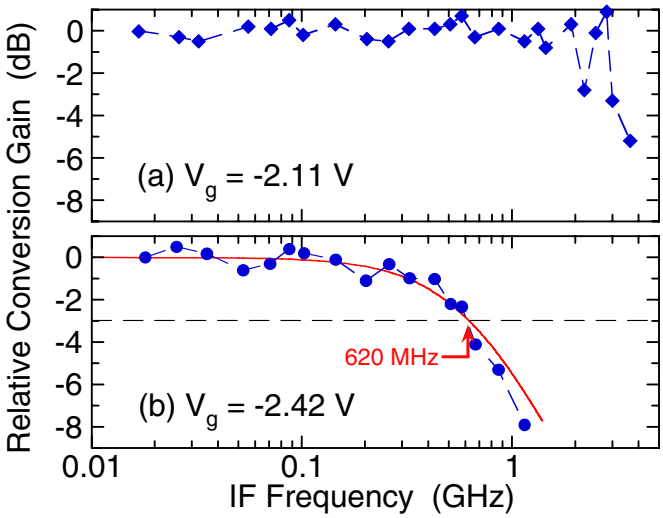

FIG. 3. IF dependence of the mixer conversion gain, normalized to 17 MHz, for a 145 GHz rf. Conversion gains are corrected for the IF amplification chain. In (a) V_g is held at the 145 GHz plasmon resonance, while in (b) V_g is held in the broadband pinch-off response (see Fig. 1). The red curve in (b) is a fit to the data using a Lorentzian, which gives a –3dB bandwidth of 620 MHz.

complicated series of harmonics of the IF, with the 2 IF harmonic smaller than but comparable to the fundamental, and detectable harmonics up to 9 IF. Fig. 2(b) shows the spectrum for the same parameters except with $V_g = –2.42$ V, in the pinch-off response. In contrast to Fig. 2(a), Fig. 2(b) is uncomplicated, consisting almost solely of the fundamental IF with only a very small 2 IF distortion. It is clear that the IF generation mechanisms for the resonant plasmon and broadband pinch-off responses are fundamentally different

Likewise, the IF bandwidth for mixing on the plasmon resonance shows basic differences from the pinch-off response. Fig. 3 shows the mixer conversion gain $\eta = P_{IF}/P_{rf}$, where P_{IF} and P_{rf} are the IF output and rf input powers at a fixed LO power of 0.1 mW, as a function of the IF with the rf set at 145 GHz. The data have been corrected for the losses and gains in the IF signal chain. The data in Fig. 3(a) is taken at $V_g = –2.11$ V, on the 145 GHz plasmon resonance. Here the IF bandwidth, defined as the IF where η falls 3 dB below its low-frequency value, significantly exceeds the 2 GHz instrumental limit, which on this plot appears as a rapidly degenerating signal-to-noise. The data in Fig. 3(b) is again the same parameters except with $V_g = –2.42$ V, in the pinch-off

response. In this regime the IF bandwidth is < 1 GHz and can be reasonably fit to a Lorentzian, which yields an IF bandwidth of 620 MHz.

To understand the physical basis of the mixing, we begin with the pinch-off regime since Figs. 2(b) and 3(b) present a simpler case compared to the plasmon regime. The fact that the IF is nearly free of harmonic distortion means that the difference frequency is generated to a high degree of accuracy by a pure cross multiplication term ($E_{LO}\cos[\omega_{LO}t] \times E_{rf}\cos[\omega_{rf}t]$). The most straightforward nonlinearity that has no higher order cross terms is a square-law response. A very pure square-law response is characteristic of bolometric mixers, which are usually broadband detectors as well. Further evidence supporting bolometric mixing near pinch-off is in the shape of the conversion gain roll-off in Fig. 3(b). For bolometric mixing the IF dependence of η should be a Lorentzian: $\eta = (1 + (f_{IF}/f_{3dB})^2)^{-1}$, where the IF bandwidth f_{3dB} is set by the thermal relaxation time. This Lorentzian shape is the basis of the fit in Fig. 3(b). The 620 MHz f_{3dB} near pinch-off is more consistent with a hot-electron bolometer (HEB),[13,14,15,16] rather than a conventional bulk bolometer which usually has f_{3dB} in the kHz to few MHz range. Finally, the definitive aspect of bolometric behavior is the proportionality between response and the resistance vs. temperature slope dR/dT. This relation is shown in Fig. 1 (inset), which plots both the responsivity at 94 GHz and dR_{DS}/dT as a function of V_G near 4 K. The responsivity tracks closely the behavior of dR_{DS}/dT as a function of V_g, both quantities being small and nearly independent of V_g for most of the range but showing a sudden large and proportionate increase at the same V_g.

The broadband pinch-off response of the DQW FET is thus best described as bolometric. This contrasts with the nonresonant direct detection near conduction threshold in a HEMT as reported in Ref. 10, which was attributed to excitation of overdamped plasmon modes. In the case of the DQW FET, electrons in the ungated QW regions between grating-gate fingers have $\omega_0\tau \approx 40$ for a 94 GHz drive, which is well into the underdamped plasmon regime defined by $\omega_0\tau > 1$. This and the bolometric signatures presented rule out overdamped plasmon response in the DQW FETs. It is certainly possible that the threshold response in the DQW FET and the HEMT result from different physical mechanisms.

The physics underlying the mixing on the plasmon resonance is significantly more difficult to analyze, so only a few general conclusions can be drawn here. It is obvious that the IF harmonics generated by plasmon mixing are incompatible with a square-law response and hence rule out bolometric mixing. In terms of nonlinear mechanisms, the cross term used in Ref. 5 to describe plasmon mixing was only the leading order term in a series expansion of field products, while Ref. 6 did not treat nonlinear response, so there exists no firm theoretical guidance on the plasmon mixing process. While the physical mechanism of the plasmon nonlinear behavior is uncertain, in general it is tied to plasmon interactions that also affect the plasmon lifetime τ_{plas}, such as plasmon-plasmon scattering or dissipation of the plasmon via phonons or electrons not in the coherent density oscillation. In such a case the IF bandwidth of a plasmon mixer should be of order $1/\tau_{plas}$. From Fig. 1, the f_0 = 145 GHz plasmon has an "electrical" Q, defined as the resonant gate voltage divided by the voltage full-width at half-maximum, of 8. The IF bandwidth would then be of order $f_0/2Q$ = 9 GHz.

It is important to note that the plasmon responsivity is very low, only about 2 mV/W. By contrast, Ref. 5 calculated that responsivities up to 10^3 V/W are possible on the resonance of an underdamped plasmon. Whether this large discrepancy arises from intrinsic reasons or correctable extrinsic reasons, such as poor radiation coupling into the 2DEG, is being investigated.

3. Electric and Magnetic Metamaterial Electrodynamic Response

Artificial materials which exhibit a designed electromagnetic (EM) response have recently generated great interest [17]. This is due in part from the ability of these materials to exhibit an EM response not readily available in naturally occurring materials such as: negative refractive index [18], artificial magnetism [19], super focusing [20,21] and reduced lens aberrations [22]. Another advantageous and distinguishing property of EM metamaterials is that resonant structures can be designed over a large portion of the electromagnetic spectrum ranging from radiofrequency [23] through the terahertz [24] and near infrared regimes [25]. Thus, regions devoid of natural material response, such as the so-called terahertz gap, can be targeted for metamaterial applications. Further, the majority of metamaterials use elements (typically highly conducting metals such as Cu,

Ag, or Au) that are common in conventional microfabrication techniques, offering considerable flexibility in the design of new structures or in the incorporation of additional functionality into existing devices.

For many potential applications, it would be desirable to create metamaterials that exhibit a controlled active, dynamical, and/or tunable response. For example, the dynamic control of metamaterial properties has been demonstrated at microwave frequencies [26]. However, while resonant metamaterials have been fabricated which operate at terahertz [24] and higher frequencies, dynamic control has yet to be demonstrated. Specifically, a dynamic metamaterial response has yet to be demonstrated at terahertz frequencies.

An issue regarding the practicality of metamaterials as devices involves their potentially complicated EM response. Many metamaterial structures (though geometrically simple) exhibit a bianisotropic response, making a full electromagnetic characterization difficult and complicating their utilization as devices. For example, the split ring resonator (SRR) was originally designed for its unique magnetic response. However, great care must be taken in characterizing or utilizing this magnetic response since, as symmetry arguments reveal, the magnetic $\mu(\omega)$ and electric $\varepsilon(\omega)$ resonances occur at the same frequency [27]. Additionally, a coupling exists between the frequency dependent electric and magnetic responses. This is characterized by off diagonal terms in the magneto-optical permittivity, and, thus, the SRR is bianisotropic [27,28]. Nonetheless, with careful characterization, such complications can be avoided or even taken advantage of, as new unique EM properties emerge for bianisotropic materials [29]. Although much work has been completed on investigation of the magnetic SRR response, the electric and magneto-optical response has yet to be fully characterized or utilized.

Here we utilize terahertz time domain spectroscopy [30] to characterize the electromagnetic response of a planar array of SRRs fabricated upon semi-insulating GaAs. In addition to characterizing both the $\mu(\omega)$ and $\varepsilon(\omega)$ responses, we demonstrate for the first time the potential for creating dynamic SRR structures. This is accomplished through photoexcitation of free carriers in the GaAs substrate, which short out the SRR gap, thereby turning off the electric resonance, demonstrating the potential of SRR-based artificial materials as terahertz switches. As mentioned, EM metamaterials have been

demonstrated over many decades of frequency. Thus, our results are not limited only to terahertz frequencies but may be used over much of the electromagnetic spectrum.

A planar array of SRRs are fabricated from 3 μm thick copper on a 670 μm thick high resistivity GaAs substrate. The outer dimension of an individual SRR is 36 μm and the unit cell is 50 μm [31]. We characterized the frequency dependent electric and magnetic response using terahertz time domain spectroscopy (THz-TDS) where the transmitted electric field is measured for the SRR sample and a suitable reference, which in this case is a bare GaAs substrate. Dividing the Fourier transformed sample and reference waveforms yields the complex transmissivity $t(\omega) = (T(\omega))^{1/2}\exp(i\phi(\omega))$ of the sample under investigation. This phase sensitive characterization further permits determination of the frequency dependent optical constants, e.g., $\varepsilon(\omega) = \varepsilon_1(\omega) + i\varepsilon_2(\omega)$, through inversion of the Fresnel equations without model assumptions. Utilization of GaAs as a substrate provides the opportunity to dope the substrate by optical excitation. This is accomplished using optical-pump terahertz probe spectroscopy [32], whereby a ~50 fs,

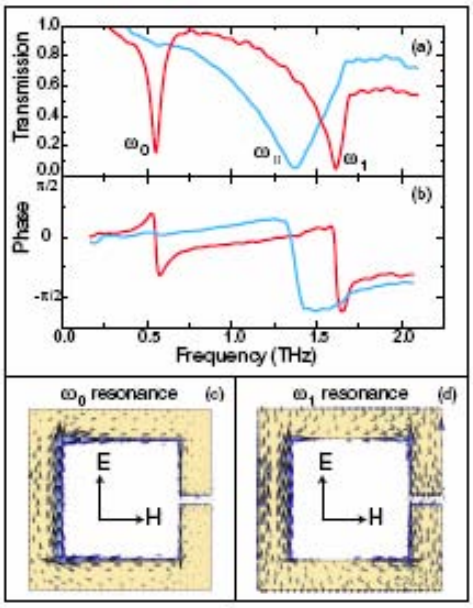

FIG. 4. The frequency dependent transmission spectra $T(\omega)$ of the SRR sample is shown in (a), and in (b) the corresponding phase of the transmission is shown. In (a) and (b), the electric field is perpendicular to the SRR gap [red curves] and parallel to the SRR gap [blue curves] at normal incidence. (c) and (d) are the surface current densities for the ω_0 (0.5 THz) and ω_1 (1.6 THz) resonances, respectively, as calculated by simulation.

800 nm pulse excites carriers across the 1.42 eV band gap in GaAs. The lifetime of the photodoped carriers is 1 ns, thus allowing for characterization of the quasi-steady state response of the SRRs as a function of the carrier density by simply changing the excitation fluence.

In the following, we first consider the SRR response without photoexcitation. In Fig. 4(a), we show the transmission spectra and, in Fig. 4(b), the corresponding phase. Since the measurements are obtained at normal incidence and the magnetic field lies completely in the SRR plane, the measurements focus solely on the electric resonant response. The red curves are the response with the electric field (**E**) polarized perpendicular to the SRR gap [depicted in Fig. 4(c)], while the blue curves are with the electric field oriented parallel to the SRR gap. On the low frequency side, the transmission is high and approaches 95% for both polarizations. With the electric field perpendicular to the SRR gap, a pronounced resonance $\omega_0 = 0.5$ THz is observed where the transmission decreases to ~15%. In addition, there is a second absorption resonance near $\omega_1 = 1.6$ THz. In order to understand the origin of the ω_0 and ω_1 resonances, we have performed numerical simulations of the SRR response using commercial code. Figures 1(c) and 1(d) show the results of the calculated surface currents at ω_0 and ω_1, respectively. The low energy ω_0 absorption, due to an electric response $\varepsilon(\omega)$ of the SRRs, occurs at the same frequency as the magnetic $\mu(\omega)$ resonance [27]. This is evidenced by the observation of the circulating currents shown in Fig. 4(c) produced from the incident time varying electric field which generates a magnetic field polarized parallel to the surface normal of the SRR. This is not surprising since, as mentioned, SRRs are bianisotropic, meaning that the electric and magnetic responses of the SRR are coupled $\varepsilon(\omega) \Leftrightarrow \mu(\omega)$. In contrast, the higher energy ω_1 resonance at 1.6 THz is from the half wave resonance due to the side length $L = 36$ μm of the SRR, consistent with the calculated surface currents shown in Fig. 4(d) [33].

Upon rotating the SRR sample by 90° such that **E** is parallel to the SRR gap, a different electrical resonant behavior is observed [blue curves in Figs. 4(a) and 4(b)]. In particular, there is only a single broad absorption at $\omega_{||} = 1.38$ THz. We have verified through simulation that this resonance is analogous to the ω_1 half wave resonance. The redshift and broadening of the $\omega_{||}$ resonance in comparison to the ω_1 is consistent with

the fact that there are now two L = 36 μm side lengths per unit cell resulting in enhanced dipolar coupling [34]. Importantly, there is no electric resonance that is analogous to the ω_0 resonance for this orientation; i.e., there is no response with **E** producing circulating currents with an associated magnetic field directed perpendicular to the GaAs substrate. This is expected as a detailed group theoretical analysis has revealed [27].

To further investigate the nature of the ω_0 resonance, the SRR response was measured at various angles of incidence. Measurements were performed with **E** parallel to the SRR gap so that there is no electrically active ω_0 resonance to complicate determination of the $\mu(\omega)$ response. In particular, the SRR is rotated about an axis parallel to the split gap of the SRR. This permits characterization of the magnetic response of the SRR since $\mu(\omega)$ increases for increasing angles with a maximum occurring for Θ = 90°. The results for angles of incidence Θ = 0, 23°, and 45° are shown in Fig. 5. The normal incidence data for **E** perpendicular to the SRR gap [from Fig. 4(a)] is replotted as a dashed red line as a reference. For normal incidence [blue curve], there is no discernible feature at 0.5 THz. However, at the incident angle Θ = 23° (black curve), a slight dip begins to develop at ω_0. The magnetic coupling to this mode can be further strengthened by increasing the incident angle, and this is apparent and for 45° [green curve], where there is a well

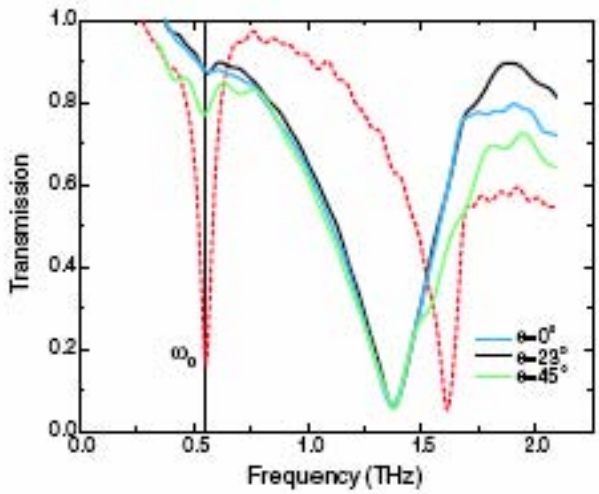

FIG. 5. Transmission spectra of the magnetic response of the SRRs. The dashed red curve is the electric response (i.e., **E** perpendicular to the SRR gap, normal incidence) replotted from Fig. 4. As the SRR is rotated about an axis parallel to the electric field, an absorption dip due to the magnetic response $\mu(\omega)$ of the SRRs is observed at ω_0.

developed absorption obvious in transmission at ~0.5 THz. This behavior is consistent with the development of a resonant $\mu(\omega)$ response since, with an increasing angle of incidence, a correspondingly larger component of the incident magnetic field is projected normal to the plane in of the SRRs (i.e., perpendicular to the GaAs substrate). In addition, as the black dashed vertical line in Fig. 5 reveals, the $\mu(\omega)$ and $\varepsilon(\omega)$ responses both occur at ω_0 as discussed above. The combined results of Figs. 1 and 2 provide a fairly complete description of the electromagnetic response of the SRRs in the absence of photoexcitation.

Finally, we focus on induced changes in the electric resonant response (i.e., ω_0 and ω_1) following photoexcitation. Since the ω_0 resonance shown in Fig. 4(a) has been shown to focus strong electric fields within the split gap of the SRR [29], it is expected that the resonance at ω_0 should strongly depend upon materials placed in or near the gap. Our approach to study the change in resonant response of the SRR is to change the background dielectric of the substrate material as a function of photodoping. The dielectric function of GaAs is changed dynamically with a ~50 fs optical pulse that creates free carriers in the conduction band. The resulting effect on the resonant SRR response is studied as a function of pump power. The pump pulse is timed to arrive 5 ps before the peak of the THz waveform, ensuring that a long-lived carrier density has been established. Since the lifetime of carriers in GaAs is significantly longer than the picosecond waveform, this allows us to characterize the quasi-steady state response of the SRRs as a function of incident power (i.e., carrier density in the GaAs substrate).

In Fig. 6(a), we show the dependence of both electric resonances ω_0 and ω_1 on pump power in transmission. The solid red curve in Fig. 6 is the response of the SRRs replotted from Fig. 4(a), i.e., the electric response of the SRRs at zero pump power. At a pump power of 0.5 mW [green curve in Fig. 6], the overall transmission decreases and the strength of the ω_0 resonance significantly weakens. In our experiment, 0.5 mW corresponds to a fluence of 1 J/cm^2 resulting in a photoexcited carrier density $n \sim 2 \times 10^{16}$ cm^3. Although ω_0 is strongly affected by pump powers as small as 0.5 mW, it is interesting to note that ω_1 is not significantly altered. When the pump power is increased to 1 mW the low energy resonance ω_0 associated with circulating currents in the SRRs is

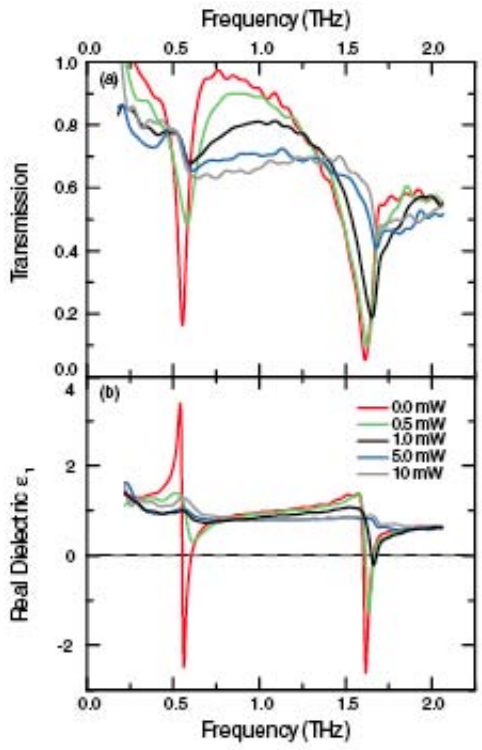

FIG. 6. (a) Transmission spectra as a function of photodoping fluence for the electric resonance of the SRRs. The polarization of the incident EM wave is as shown in Fig. 4(c). As the power is increased, the first mode is shorted out and the overall transmission decreases. At higher powers, the second mode can also be seen to die off. (b) Corresponding change of the real dielectric constant ε_1 of the SRRs as a function of power.

nearly entirely quenched. In this case, the transmission at ω_0 increases from ~15% to over 70%. Further, $T(\omega)$ continues to decrease over all frequencies characterized which is due, in part, to the free carrier response of the photoexcited GaAs. Notice that, although ω_0 has been short-circuited, there is still little change in ω_1. At 5 mW of pump power, $T(\omega)$ further decreases and finally ω_1 begins to weaken.

The dependence of ω_0 and ω_1 on pump power can be understood by considering the different nature of these two resonances. As mentioned, the lower energy resonance is attributed to circulating currents within the SRR. Thus, by providing free charges within the substrate, it becomes possible to short-circuit the response and, as the gap in the SRR is relatively small (~2 μm), only low pump powers are required. However, ω_1 is due to the side length of the SRR, and, therefore, more charges (and thus more power) are required to effectively screen this resonance.

We now discuss the real part of the dielectric function $\varepsilon_1(\omega)$, displayed in Fig. 6(b). This further highlights that, for low excitation densities, the ω_0 resonance completely disappears, while the ω_1 survives to slightly higher fluences. Notice, for zero pump power, the SRR metamaterials obtain a region of negative $\varepsilon_1(\omega)$ for both the ω_0 and ω_1 resonances. The region of negative $\varepsilon_1(\omega)$ for ω_0 spans from 550 to 600 GHz and reaches a maximum negative value of –2.5 at 560 GHz, while ω_1 spans from 1.6 to 1.66 THz and obtains a slightly greater value of –2.6. For a pump power of 0.5 mW, the ω_0 resonance is reduced greatly and the $\varepsilon_1 < 0$ response destroyed. Thus, one scenario permitting these metamaterials to be used as dynamical devices involves a photoinduced bandpass response. For example, if used at 560 GHz, where the transmission has a minimum, a 1 mW pump pulse increases $T(\omega)$ by ~60% and, consequently, changes the SRR metamaterial medium from absorbing to transparent.

The results of Fig. 6 were obtained for SRRs fabricated on intrinsic GaAs substrates. In this case, the recombination time of the carriers in GaAs is greater than 1 ns, meaning that the switched state of the SRR structure (i.e., the photoinduced increase in transmission) is long-lived. However, it would be possible to fabricate identical SRR structures on low temperature grown gallium arsenide or GaAs:ErAs semiconductor heterostructures [35], the latter of which allows for engineered picosecond (1 to 10 ps) carrier recombination times. This would enable picosecond on/off switching times of the SRR electric response, enabling optically controlled high frequency modulation of narrow band high-frequency sources. Furthermore, with electrical carrier injection, another possibility would be to create all-electrical high-frequency modulators.

4. References

[1] S. J. Allen, D. C. Tsui, R. A. Logan, Phys. Rev. Lett. **38**, 980 (1977)

[2] D. C. Tsui, E. Gornik, R. A. Logan, Solid. State Comm. **5**, 875 (1980)

[3] P. J. Burke, I. B. Spielman, J. P. Eisenstein, L. N. Pfeiffer, K. W. West, Appl. Phys. Lett. **76**, 745 (2000)

[4] M. I. Dyakonov, M. S. Shur, Phys. Rev. Lett. **71**, 2465 (1993)

[5] M. I Dyakonov, M. S. Shur, IEEE Trans. Elec. Devices **43**, 380 (1996)

[6] V. V. Popov, O. V. Polischuk, T. V. Teperik, X. G. Peralta, S. J. Allen, N. J. M Horing, M. C. Wanke, J. Appl. Phys. **94**, 3556 (2003)

[7] W. Knap, J. Lusakowski, T. Parenty, S. Bollaert, A. Cappy, V. V. Popov, M. S. Shur, Appl. Phys. Lett. **84**, 2331 (2004)

[8] X. G. Peralta, S. J. Allen, M. C. Wanke, N. E. Harff, J. A. Simmons, M. P. Lilly, J. L. Reno, P. J. Burke, J. P. Eisenstein, Appl. Phys. Lett. **81**, 1627 (2002)

[9] W. Knap, Y. Deng, S. Rumyantsev, J.-Q. Lu, M. S. Shur, C. A. Saylor, L. C. Brunel, Appl. Phys. Lett. **80**, 3433 (2002); W. Knap, Y. Deng, S. Rumyantsev, M. S. Shur, Appl. Phys. Lett. **81**, 4637 (2002)

[10] W. Knap, V. Kachoroskii, Y. Deng, S. Rumyantsev, J.-Q. Lu, R. Gaska, M. S. Shur, G. Simin, W. Hu, M. Asif Khan, C. A. Saylor, L. C. Brunel, J. Appl. Phys. **91**, 9346 (2002)

[11] T. Otsuji, M. Hanabe, O. Ogawara, Appl. Phys. Lett. **85**, 2119 (2004)

[12] W. Knap, F. Teppe, Y. Meziani, N. Dyakonova, J. Lusakowski, F. Boeuf, T. Skotnicki, D. Maude, S. Rumyantsev, M. S. Shur, Appl. Phys. Lett. **85**, 675 (2004)

[13] M. Lee, L. N. Pfeiffer, K. W. West, Appl. Phys. Lett. **81**, 1243 (2002)

[14] J. Kawamura, R. Blundell, C. E. Tong, G. Golt'sman, E. Gershenzon, B. Voronov, S. Cherednichenko, Appl. Phys. Lett. **70**, 1619 (1997)

[15] K. S. Yngvesson, Appl. Phys. Lett. **76**, 777 (2000)

[16] M. Lee, L. N. Pfeiffer, K. W. West, K. W. Baldwin, Appl. Phys. Lett. **78**, 2888 (2001)

[17] D. R. Smith, W. J. Padilla, D. C. Vier, S.C. Nemat-Nasser, and S. Schultz, Phys. Rev. Lett. **84**, 4184 (2000)

[18] V. G. Veselago, Sov. Phys. Usp. **10**, 509 (1968)

[19] J. B. Pendry, A. J. Holden, D. J. Robbins, and W. J. Stewart, IEEE Trans. Microwave Theory Tech. **47**, 2075 (1999)

[20] J. B. Pendry, Phys. Rev. Lett. **85**, 3966 (2000)

[21] R. A. Shelby, D.R. Smith, and S. Schultz, Science **292**, 77 (2001)

[22] D. Schurig and D. R. Smith, Phys. Rev. E **70**, 065601(R) (2004)

[23]M. C. K. Wiltshire, J. B. Pendry, I. R. Young, D. J. Larkman, D. J. Gilderdale, and J.V. Hajnal, Science **291**, 849 (2001)

[24] T. J. Yen, W. J. Padilla, N. Fang, D. C. Vier, D.R. Smith, J. B. Pendry, D.N. Basov, and X. Zhang, Science **303**, 1494 (2004)

[25]S. Zhang, W. Fan, N. C. Panoiu, K. J. Malloy, R. M. Osgood, and S. R. J. Brueck, Phys. Rev. Lett. **95**, 137404 (2005)

[26] S. Lim, C. Caloz, and T Itoh, IEEE Trans. Microwave Theory Tech. **52**, 2678 (2004)

[27] W. J. Padilla, cond-mat/0508307

[28] R. Marque´s, F. Medina, and R. Rafii-El-Idrissi, Phys. Rev. B **65**, 144440 (2002)

[29] J. B. Pendry, Science **306**, 1353 (2004)

[30] D. Grischkowsky, S. Keiding, M. van Exter, and Ch. Fattinger, J. Opt. Soc. Am. B **7**, 2006 (1990)

[31] The dimensions used for the SRR samples are identical to those for sample D3 in Ref. 24.

[32] R. D. Averitt and A. J. Taylor, J. Phys. Condens. Matter **14**, R1357 (2002)

[33] The resonant frequency is approximately determined by $\omega_l \approx (2 \text{ x } 36\ \mu\text{m})\langle\varepsilon\rangle^{1/2}$, where $\langle\varepsilon\rangle$ is the average dielectric constant near the gap of the SRR.

[34] W. Rechberger, A. Hohenau, A. Leitner, J.R. Krenn, B. Lamprecht, and F. R. Aussenegg, Opt. Comm. **220**, 137 (2003)

[35] R. P. Prasankumar, A. Scopatz, D. J. Hilton, A. J. Taylor, R. D. Averitt, J. M. Zide, and A. C. Gossard, Appl. Phys. Lett. **86**, 201107 (2005)

Distribution

1	MS 0123	LDRD Office, 1030
1	MS 1071	J. F. Jakubczak, 1720
1	MS 1079	G. V. Herrera, 1700
1	MS 1082	M. C. Wanke, 1725
1	MS 1082	J. J. Hudgens, 1725
1	MS 1086	D. L. Barton, 1123
1	MS 1086	1123 Department File
1	MS 1303	J. L. Reno, 1132
5	MS 1415	M. Lee, 1123
1	MS 1415	C. Highstrete, 1123
1	MS 1415	E. A. Shaner, 1123
1	MS 1415	J. C. Barbour, 1120
1	MS 1415	R. Q. Hwang, 1110
1	MS 1421	J. A. Simmons, 1130
1	MS 1427	J. M. Phillips, 1100

1	MS 0161	Patent and Licensing Office, 1150
2	MS 0899	Technical Library, 4536
2	MS 9018	Central Technical Files, 8944